Higher atmospheric aridity-dominated drought stress contributes to aggravating dryland productivity loss under global warming

Article *in* Weather and Climate Extremes · May 2024

DOI: 10.1016/j.wace.2024.100692

Xiaojing Yu
Xinjiang University

Lixia Zhang
Institute of Atmospheric Physics, Chinese Academy of Sciences

Tianjun Zhou
Chinese Academy of Sciences

Jianghua Zheng
Xinjiang University

Weather and Climate Extremes 44 (2024) 100692

Contents lists available at ScienceDirect

Weather and Climate Extremes

journal homepage: www.elsevier.com/locate/wace

Higher atmospheric aridity-dominated drought stress contributes to aggravating dryland productivity loss under global warming

Xiaojing Yu [a,b], Lixia Zhang [c,b,*], Tianjun Zhou [c,d], Jianghua Zheng [a], Jingyun Guan [e]

[a] *College of Geography and Remote Sensing Sciences, Xinjiang University, 830017 Urumqi, China*

[b] *Collaborative Innovation Center on Forecast and Evaluation of Meteorological Disasters, Nanjing University of Information Science and Technology, 210044, Nanjing, China*

[c] *State Key Laboratory of Numerical Modeling for Atmospheric Sciences and Geophysical Fluid Dynamics (LASG), Institute of Atmospheric Physics, Chinese Academy of Sciences, 10029, Beijing, China*

[d] *University of Chinese Academy of Sciences, 10049, Beijing, China*

[e] *College of Tourism, Xinjiang University of Finance and Economics, 830012, Urumqi, China*

A R T I C L E I N F O

Keywords:
Drought stress
High vapor pressure deficit (VPD)
Dryland productivity
CMIP6 projections
Global warming

A B S T R A C T

Dryland ecosystems are highly vulnerable to extreme droughts under climate change. Yet, response of vegetation productivity across global drylands to changes in drought stress in a warming climate remains obscure. Here, we investigated future changes in drought stress, characterized by low soil moisture (SM) and high vapor pressure deficit (VPD), under severe drought conditions and its impact on gross primary productivity (GPP) deviations in drylands, based on the Coupled Model Intercomparison Project Phase 6 (CMIP6) Earth system model (ESM) simulations. Under both intermediate (SSP2-4.5) and high (SSP5-8.5) emission scenarios, the dryland ecosystems are projected to experience more intense, extensive and frequent severe drought events owing to increasing VPD. The probabilities of high VPD-dominated drought stress in the end of the 21st century would be nearly double (2.1–2.4 times) of the present-day (39%). Excluding the carbon dioxide (CO_2) fertilization effect, the annual GPP loss caused by severe drought is projected to further deteriorate over more than half fraction (56.9–70.9%) of global vegetated dryland areas, reaching 2.0 (1.9–2.2) times of the present-day (with an area-weighted total of -21.5 KgC m^{-2} yr^{-1}) by the end of the 21st century. Such aggravating reduction is predominantly induced by drought stress with higher-than-usual VPD anomaly. The high VPD-dominated drought stress would lead to approximately 100% (95–102%) of annual aggregated dryland GPP loss by the end of 21st century from the present-day 68%. Our results suggest an increasing risk of high atmospheric aridity-dominated drought stress on dryland ecosystems. It is of great urgency to make adaption and mitigation strategies for the natural and cultivated vegetation in drylands.

1. Introduction

Drylands are typically characterized by scarce and erratic precipitation and high evaporation loss. Hosting roughly 20% of global plant diversity hotspots and 44% of global cropland areas (White and Nackoney 2003; Davies et al., 2016), dryland ecosystems contribute up to ~40% of global carbon uptake (Wang L et al., 2022; Wang S et al., 2023) and are crucial to global food security (Fu et al., 2021). Severe drought heavily impinges the physiological functioning of natural and cultivated plants during the growing season (Reichstein et al., 2013; Gentine et al., 2019; Piao et al., 2019), further leading to detriment impacts on ecological and social systems, such as tree mortality (Hammond et al., 2022; Yi et al., 2022), wildfire activity (Jain et al., 2022; Jones et al., 2022) and agricultural yield loss (Lobell et al., 2014; Kimm et al., 2020). Under climate change, drylands have experienced a more evident warming amplified by the land-atmosphere feedback (Huang et al., 2017). For their vulnerability and low resilience, ecosystems across the water-scarce drylands are susceptible to threats from severe drought stress (Davies et al., 2016). Therefore, understanding future changes in drought stress and their adverse impacts on dryland ecosystems under global warming help inform to facilitate mitigation and adaption management for carbon neutrality and sustainable development goals

* Corresponding author. State Key Laboratory of Numerical Modeling for Atmospheric Sciences and Geophysical Fluid Dynamics (LASG), Institute of Atmospheric Physics, Chinese Academy of Sciences, Beijing 10029, China

E-mail address: lixiazhang@mail.iap.ac.cn (L. Zhang).

https://doi.org/10.1016/j.wace.2024.100692
Received 22 October 2023; Received in revised form 19 March 2024; Accepted 17 May 2024
Available online 17 May 2024

Table 1
Information of CMIP6 ESMs used in this study.

No.	Model Name	Institute, Country	Horizontal Resolution (Lat × Lon, grid points)	Land surface model and vegetation model	Dynamic vegetation model	References
1	BCC-CSM2-MR	Beijing Climate Center (BCC), China	160 × 320	BCC Atmosphere–Vegetation Interaction Model version 2.0 (BCC-AVIM2)	Yes	Wu et al. (2019)
2	CanESM5	Canadian Centre for Climate Modelling and Analysis (CCCma), Canada	64 × 128	Coupled Canadian Land Surface Scheme and the Canadian Terrestrial Ecosystem Model (CLASS-CETM)	Yes	Swart et al. (2019)
3	CMCC-CM2-SR5	The Euro-Mediterranean Centre on Climate Change (CMCC)	192 × 288	Community Land Model version 4.5 (CLMv4.5)	Yes	Cherchi et al. (2019)
4	EC-Earth3-CC	EC-Earth-Consortium, Europe	256 × 512	Hydrology Tiled ECMWF Scheme of Surface Exchanges over Land (HTESSEL) and Lund-Potsdam-Jena General Ecosystem Simulator (LPJ-GUESS)	Yes	Döscher et al. (2022)
5	EC-Earth3-Veg		256 × 512			
6	EC-Earth3-Veg-LR		160 × 320			
7	IPSL-CM6A-LR	Institute Pierre Simon Laplace (IPSL), France	143 × 144	Organizing Carbon and Hydrology in Dynamic Ecosystems (ORCHIDEE) version 2	Yes	Boucher et al. (2020)
8	MPI-ESM1-2-HR	Max Planck Institute for Meteorology (MPI-M), Germany	192 × 384	Jena Scheme for Biosphere-Atmosphere Coupling in Hamburg version 3.2 (JSBACH3.2)	Yes	Mauritsen et al. (2019)
9	MPI-ESM1-2-LR		96 × 192			

(SDGs).

Gross primary productivity (GPP), the carbon flux entering biosphere from the atmosphere via vegetation photosynthesis, is crucial for understanding global carbon cycle and estimating terrestrial carbon uptake (Cox and Jones, 2008; Running, 2008). Drought conditions contribute to approximately half fraction of global GPP reduction linked to climate extremes (Gampe et al., 2021). The direct drought stress on plant physiological function basically comes from reduced soil water supply, measured by soil moisture (SM), and high evaporative demand, measured by vapor pressure deficit (VPD), respectively. Under such conditions, xylem conduits and the rhizosphere cavitate, resulting in stopping the flow of water and desiccating plant tissues (i.e., "hydraulic failure" hypothesis); meanwhile, stomatal closure to prevent hydraulic failure causes photosynthetic uptake of carbon dioxide (CO_2) to diminish and the plant starves (i.e., "carbon starvation" hypothesis) (McDowell et al., 2008, 2022; McDowell, 2011; Grossiord et al., 2020; Novick et al., 2024). Both satellite observations and Earth system model (ESM) simulations have showed the vital roles of both SM and VPD in regulating the variations of global carbon uptake (Green et al., 2019; Liu et al., 2020; Xu et al., 2023) and vegetation growth (Yuan et al., 2019; He et al., 2022). Particularly, the response direction of vegetation productivity to atmospheric aridity would reverse when VPD surpasses a certain threshold during growing season (He et al., 2023; Zhong et al., 2023). Furthermore, the strong land–atmosphere feedbacks intensify atmospheric aridity and soil drought on a monthly scale (Berg et al., 2016; Zhou et al., 2019a), further exacerbating their detrimental impacts on terrestrial ecosystems (Zhou et al., 2019b; Humphrey et al., 2021).

Under the greenhouse gases (GHG) induced warming, severe droughts accompanied with substantial rise in VPD and drying in SM have spread throughout the globe over the past decades and are expected to continue in the coming century, especially in dry regions (Berg and Sheffield, 2018; Cook et al., 2020; Li et al., 2021; Fang et al., 2022). Despite the widespread greening over drylands benefit from the CO_2 fertilization effect (He et al., 2019; Gonsamo et al., 2021), the probability of drought stress dominated by high VPD has been doubled, whilst that linked with deficient SM decreased by 10% in the past two decades (Yu et al., 2023). As projected under different GHG emission scenarios, the arid and semi-arid areas might experience a more significant increase in terrestrial GPP loss induced by more frequent extreme droughts (Xu et al., 2019; Cao et al., 2022). Nonetheless, the changes in drought stress configuration and their respective influences on dryland ecosystems under climate warming remain unclear. Therefore, we here attempt to address the following questions: In a warming climate, 1) how will the two main drought stressors associated with severe drought alter across the vegetated drylands? 2) how will dryland GPP respond to such changes in severe drought stress?

2. Data and methods

2.1. Study area

In this study, we measure the spatial extent of global drylands by the widely-used aridity index (AI; Middleton and Thomas, 1992; Hulme, 1996). The global drylands are identified as regions with the AI climatology for 1961–2020 less than 0.65 (blue lines in Fig. S1), which is yielded as the ratio of annual precipitation (P) to potential evapotranspiration (PET) using the Climatic Research Unit gridded Time Series Version 4.06 (CRU TS v.4.06, Harris et al., 2020). As illustrated from the Moderate Resolution Imaging Spectroradiometer (MODIS) landcover dataset (Friedl and Sulla-Menashe, 2015), the dryland landcover types mainly include shrubs, savannas grasslands, crops and barren regions (Fig. S1), with a climatologically annual GPP amount of ~423 gC m^{-2} yr^{-1} (Fig. S2a) as estimated by the FLUXCOM datasets (Jung et al., 2019). To investigate the changes in the dryland ecosystem productivity under severe drought conditions, we further exclude the barren or sparse regions (number 16 in Fig. S1) in the study area.

2.2. CMIP6 earth system models (ESMs)

We used monthly outputs from the current Coupled Model Intercomparison Project Phase 6 (CMIP6, Eyring et al., 2016). Given the availability of GPP (variable name: gpp), surface (0–10 cm) SM (mrsos), precipitation (pr) and relevant variables for the PET calculation (details in the subsequent section), we finally selected nine ESMs from the CMIP6 archive (Table 1). GPP in each ESM was predicted by its land surface model (LSM) with a dynamic global vegetation model (DGVM). The simulation can reasonably reflect the primary spatio-temporal characteristics of dryland GPP (Figs. S2–3; Zhang Y et al., 2022). The datasets include historical simulations (1850–2014) and future projections (2015–2 100) under the combined scenarios of the Shared Socioeconomic Pathways (SSP) and the Representative Concentration Pathways (RCP), i.e., the intermediate (SSP2-4.5) and high (SSP5-8.5) GHG emission scenarios (O'Neill et al., 2016, 2017). Following the Sixth

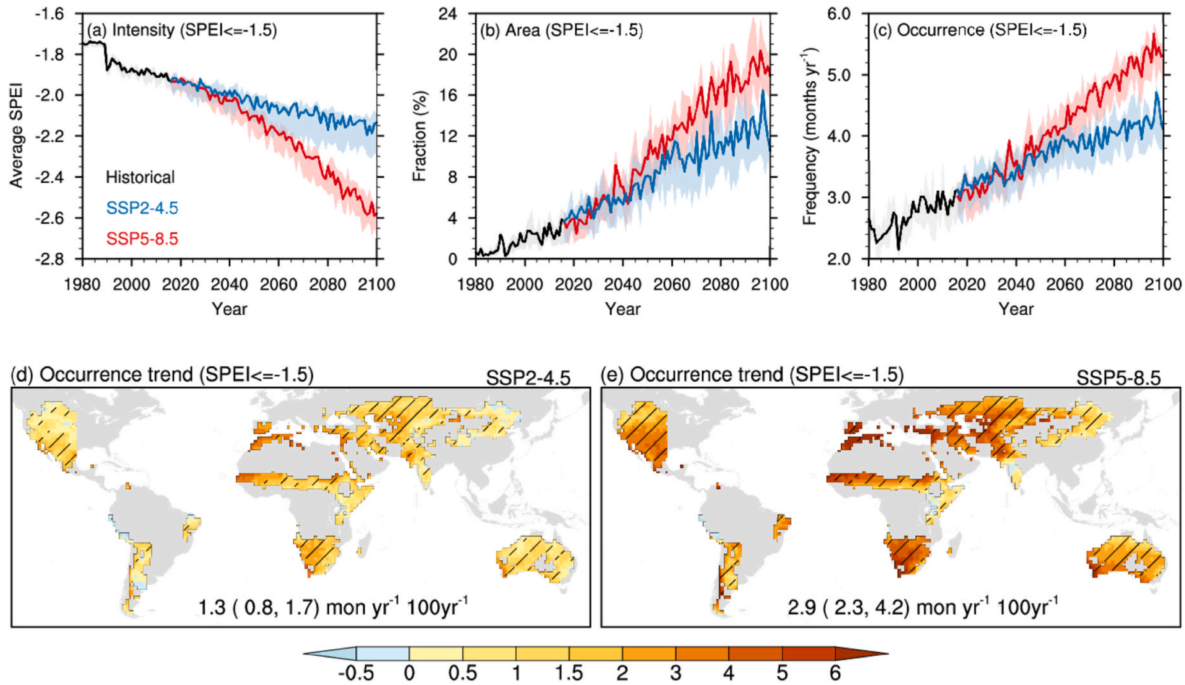

Fig. 1. Changes in severe drought characteristics across global vegetated drylands simulated by nine CMIP6 ESMs. Time series show the area-averaged (a) intensity, (b) fraction area (units: %) and (c) occurrence (units: month yr^{-1}) of severe drought events (SPEI ≤ -1.5) during 1980–2 100. Historical simulations (black) and future projections under SSP2-4.5 (blue) and SSP5-8.5 (red) scenarios are illustrated in median (solid lines) and inter-quartile ranges (shadings). (d–e) Spatial pattern of linear trends for the period 2015–2 100 in severe drought occurrence (units: mon yr^{-1} $100yr^{-1}$) under SSP2-4.5 (d) and SSP5-8.5 (e) scenarios. Slant hatchings denote where six of nine models agree in the sign of tendency. The numbers are the multi-model ensemble (MME), minimum and maximum for the area-averaged trend across global vegetated drylands.

Assessment Report (AR6) of the Intergovernmental Panel on Climate Change (IPCC) (Chen et al., 2021), we selected the first available realization of each model for each scenario to quantity the range in multi-model projections, and particularly focused on four specific periods, referred to as present-day (1995–2014), near-term (2021–2040), mid-term (2041–2060), and long-term (2081–2 100), respectively. To facilitate calculation and analysis, all outputs are first bilinearly regridded to the horizontal resolution of $1.5^\circ \times 1.5^\circ$.

2.3. Representation of severe drought conditions

We employed the Standardized Precipitation Evapotranspiration Index (SPEI) to identify severe drought conditions which is recommended to assess agricultural and ecological droughts by IPCC AR6 (Seneviratne et al., 2021). SPEI can be obtained based on a log-logistic probability distribution of the cumulative water balance (precipitation minus potential evapotranspiration, P–PET) at different time scales (Vicente-Serrano et al., 2010). In this study, monthly PET was first derived according to the Penman-Monteith approach (Penman, 1948; Monteith, 1965), following the Food and Agricultural Organization (FAO) of the United Nations (Allen et al., 1998). The input variables include the near-surface air temperature (tas), relative humidity (hurs), 10 m wind speed (uas, vas), longwave (rlds, rlus), and shortwave (rsds, rsus) radiation from CMIP6 outputs. The detailed calculation is as follows:

$$\mathrm{PET} = \frac{0.408\Delta(R_\mathrm{n} - G) + \gamma \frac{900}{T_{as}+273} u_2 (e_s - e_a)}{\Delta + \gamma(1 + 0.34u_2)} \tag{1}$$

$$e_s = 0.6108 \times \exp\left(\frac{17.27 \times T_{as}}{T_{as} + 237.3}\right) \tag{2}$$

$$e_a = e_s \times \frac{RH}{100} \tag{3}$$

where PET (mm d^{-1}) is the reference evapotranspiration rate, R_n (MJ m^{-2} h^{-1}) and G (MJ m^{-2} h^{-1}) are the net radiation and soil heat flux, respectively. T_as (°C) is 2 m air temperature, u_2 (m s^{-1}) is 2 m wind speed, Δ (kPa $^\circ C^{-1}$) represents the slope of the saturation vapor pressure–temperature relationship, and γ (kPa $^\circ C^{-1}$) is the psychrometric constant. e_s (kPa) and e_a (kPa) represents saturation vapor pressure (e_s) and actual vapor pressure (e_a), respectively, and RH (%) is relative humidity.

Because the maximum correlation between arid vegetation growth and SPEI is found at 3 to 6-month timescale (Vicente-Serrano et al., 2013), we use the 6-month SPEI (SPEI-06) to identify severe drought conditions. Using simulated precipitation (P) and derived PET, the aggregated water balance in a given month n at 6-month timescale was calculated as follows:

$$\mathrm{D}_n^k = \sum_{i=0}^{k-1} (\mathrm{P}_{n-i} - \mathrm{PET}_{n-i}), n \geq k \tag{4}$$

where D_n^k (mm) is the accumulated P–PET in a given month n, k is time scale and equals to 6 here.

Finally, we obtained SPEI-06 based on a fitted log-logistic probability distribution of D_n^k. Based on the thresholds of SPEI for drought categories, severe drought condition is identified as SPEI-06 less than −1.5 for each grid and each month (Vicente-Serrano et al., 2010).

2.4. Drought stress metrics

In this study, the two drought stressors are measured by surface SM and VPD, respectively, and the dryland ecosystem productivity is assessed by GPP, align with previous studies (Zhou et al., 2019b; Yu et al., 2023). We calculated monthly VPD values as the difference between saturation vapor pressure (e_s) and actual vapor pressure (e_a), according to Eqs. (2) and (3) and (5):

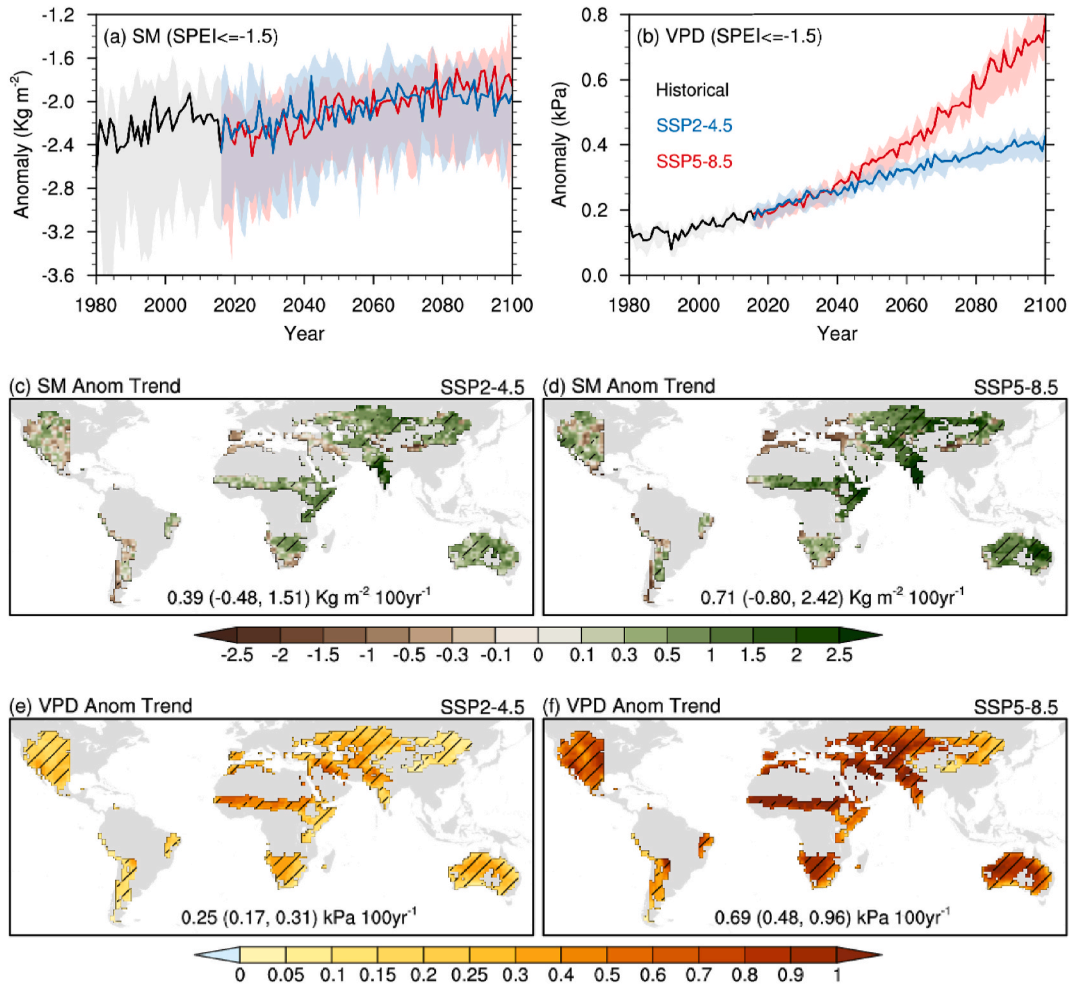

Fig. 2. Changes in the two drought stressors across global vegetated drylands simulated by nine CMIP6 ESMs. (a–b) Time series of the area-averaged anomalies of SM (a, units: Kg m^{-2}) and VPD (b, unit: kPa) associated with severe drought (SPEI ≤ -1.5) during 1980–2 100. Historical simulations (black) and future projections under SSP2-4.5 (blue) and SSP5-8.5 (red) scenarios are illustrated in median (solid lines) and interquartile ranges (shadings). (c–f) Spatial pattern of future linear trends for the period 2015–2 100 in the anomalous SM (c–d, units: Kg m^{-2} 100yr^{-1}) and VPD (e–f, units: kPa 100yr^{-1}) associated with severe drought under SSP2-4.5 (c, e) and SSP5-8.5 (d, f) scenarios. Slant hatchings denote where six of nine models agree in the sign of tendency. The numbers are the multi-model ensemble (MME), minimum and maximum for the area-averaged trend across dryland ecosystem areas.

$$\mathrm{VPD} = e_s - e_a \tag{5}$$

To exclude seasonal cycle, the anomaly for each variable was first converted as following:

$$\mathrm{Anom}_{i,j} = x_{i,j} - \overline{x_j}, \tag{6}$$

where i is the year ranging from 1980 to 2100, j is the month ranging from January to December, $x_{i,j}$ is variables of month j for year i, and $\overline{x_j}$ is the climatology for month j.

Note that the baseline for SM and VPD is 1981–2010, while GPP anomaly is relative to a running 30-year climatology from 1980 to 2 100 to adjust the general increase of GPP due to the CO_2 fertilization (Xu et al., 2019; Gonsamo et al., 2021). This approach is also efficient to exclude the primary model system biases of CMIP6 simulations (Yu et al., 2024). The anomalies of SM, VPD and GPP during severe drought conditions, representing the intensity of drought stress and the magnitude of GPP loss, respectively, were then extracted and analyzed.

To obtain an overall estimation of annual aggregated GPP deviation, we calculate an area-weighted sum of GPP anomalies across all grid points in drylands, which has been widely used in the heatwave studies (Perkins-Kirkpatrick and Lewis, 2020; Zhang et al., 2023). The calculation is as follows:

$$\text{Annual aggregated GPP deviation} = \sum\nolimits_1^g wgt \sum\nolimits_1^m \mathrm{Anom}_{j,k} \tag{7}$$

where $\mathrm{Anom}_{j,k}$ is the GPP anomaly of month j for grid k, g is the number of land grid points, and wgt is the cosine weight in the latitude direction, m is 12 months.

This method integrates into a single number all the characteristic (intensity, occurrence and spatial extent) of GPP loss/surplus related with severe drought conditions, and thus facilitates easier comparisons of GPP deviations among different years across global vegetated drylands.

Throughout the whole text, we estimated the linear trend over the period 2015–2 100 using the Theil-Sen non-parametric method (Sen, 1968; Theil, 1992), and tested the significance of monotonic trend using the Mann-Kendall (M-K) method (Mann, 1945; Kendall, 1955).

3. Results

3.1. Projected changes in the severe drought stress on dryland ecosystems

We first examine future changes in severe drought characteristics across global vegetated drylands under intermediate and high emission scenarios in terms of intensity, fraction area and frequency (Fig. 1). The

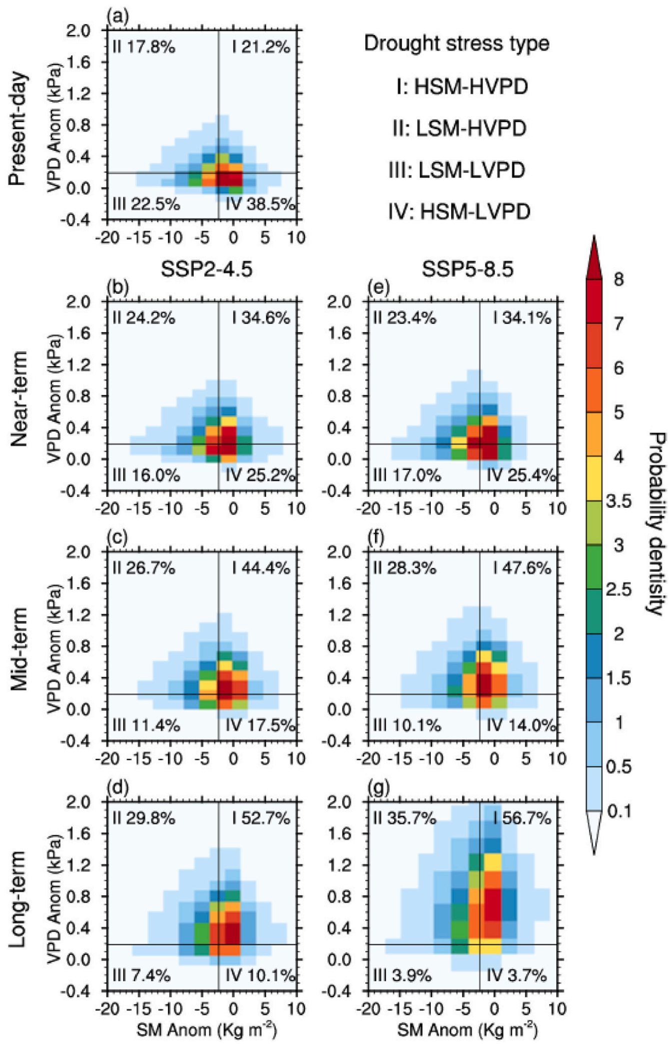

Fig. 3. Bivariate probability density functions (PDFs) for SM and VPD anomalies associated with severe drought events (SPEI ≤ -1.5) across global vegetated drylands simulated by nine CMIP6 ESMs. The results are estimated for four specific period, including the present-day period (1995–2014, a) from historical simulations, and the near-term (2021–2040, b, e), mid-term (2041–2060, c, f) and long-term (2081–2100, d, g) period from projections under SSP2-4.5 (b–d) and SSP5-8.5 (e–g) scenarios. The horizontal and vertical axises present the anomaly of SM (units: Kg m^{-2}) and VPD (unit: kPa), respectively. The thin black lines denote the present-day area-averaged anomalies of SM (-2.35 kg m^{-2}) and VPD (0.19 kPa) associated with severe droughts (Fig. S2). The numbers in the four quadrants are the percentage of the corresponding category of combined SM-VPD anomalies. The four categories refer to I: high SM and high VPD (HSM-HVPD), II: low SM and high VPD (LSM-HVPD), III: low SM and low VPD (LSM-LVPD), IV: high SM and low VPD (HSM-LVPD).

dryland ecosystems are projected to experience more intense, widespread and frequent severe drought events under future warming climate (Fig. 1a–c). All the three metrics for severe droughts present a significant increase during the 21st century under SSP2-4.5 and SSP5-8.5, but tend to rise more rapidly after the 2040s under the high emission scenario. As estimated from the multi-model ensemble (MME), the severe drought intensity is projected to increase from -1.9 at present-day to -2.1 (-2.5) in the long-term period under SSP2-4.5 (SSP5-8.5), with the fractional area rising from ~2.0% to 12.3% (18.0%) and the occurrence from 2.8 months yr^{-1} to 4.2 months yr^{-1} (5.2 months yr^{-1}). The spatial patterns for the projected trend in the severe drought occurrence (Fig. 1d and e) demonstrate a robust increasing across the vegetated drylands, with an area-averaged rate at 1.3 (0.8–1.7) months yr^{-1} 100yr^{-1} and 2.9 (2.3–4.2) months yr^{-1} 100yr^{-1} under SSP2-4.5 and SSP5-8.5, respectively. The risk of severe droughts is particularly high for the Sahel and Mediterranean costal drylands, the central Asia, South Africa, and southwestern Australia, with a rate exceeding 6.0 months yr^{-1} 100yr^{-1} under SSP5-8.5.

We extend our analysis to the two drought stressors of dryland GPP characterized by negative SM and positive VPD anomalies in Fig. 2a and b. Under SSP2-4.5 and SSP5-8.5, the MME of SM deficit associated with severe drought is projected to be relieved from -2.1 kg m^{-2} at present to about -1.9 kg m^{-2} by the end of 21st century, with the MME linear trend statistically significant at 1% level ($p = 1.0$) using the M-K test. In contrast, the atmospheric dryness will intensify continuously with the VPD anomaly in MME rising from the present-day ~0.16 kPa–0.40 kPa (0.67 kPa) under SSP2-4.5 (SSP5-8.5). The spatial distribution of the projected SM anomaly related with severe drought show a generally wetting trend over most vegetated drylands, with an area-averaged tendency of 0.39 (-0.48 to 1.51) Kg m^{-2} 100yr^{-1} and 0.71 (-0.8 to 2.42) Kg m^{-2} 100yr^{-1} under SSP2-4.5 and SSP5-8.5, respectively (Fig. 2c and d). This indicates that SM deficit caused drought stress in most dryland will alleviate. Regionally, the central Asian, South Asian, Sahel and Australian drylands would experience exacerbating SM deficit conditions, with a drying trend of -0.5 (-2.0) Kg m^{-2} 100yr^{-1} under SSP2-4.5 (SSP5-8.5). By contrast, the widespread increasing of VPD anomaly suggests an intensifying atmospheric aridity stress on dryland vegetation, with an area-averaged rate of 0.25 (0.17–0.31) kPa 100yr^{-1} and 0.69 (0.48–0.96) kPa 100yr^{-1} under SSP2-4.5 (SSP5-8.5) scenario (Fig. 2e and f). Particularly, VPD anomaly rises at a rate of ~0.3 (~1.0) kPa 100yr^{-1} over central Asian, Sahel, South African and Australian drylands under SSP2-4.5 (SSP5-8.5).

Since SM and VPD are strongly coupled at monthly scale, we further investigate their changes under severe drought in terms of the joint probability density function (PDF). The bivariate PDF distributions for SM and VPD anomalies linked with severe droughts throughout the vegetated drylands for the four periods under SSP2-4.5 and SSP5-8.5 scenarios are illustrated in Fig. 3. Overall, the density maximum tends to shift from the bottom-right (Fig. 3a) to the top-right quadrant (Fig. 3b–g) with time and warming. With respect to the present-day climatology (Fig. S4 and thin black lines in Fig. 3), we then divided the configurations of combined SM and VPD anomalies associated with severe droughts into four categories. They are termed as high SM and high VPD (HSM-HVPD), low SM and high VPD (LSM-HVPD), low SM and low VPD (LSM-LVPD), high SM and low VPD (HSM-LVPD), respectively.

From the perspective of probabilities in the four drought stress categories, the two types with higher-than-usual VPD anomaly (HSM-HVPD and LSM-HVPD) are projected to increase substantially with warming over the vegetated drylands. Of the four categories, the HSM-HVPD type is projected to occur with the largest probability, followed by the LSM-HVPD type. Specifically, the likelihood of the HSM-HVPD type (top-right quadrant) increases from the present-day 21.2% (Fig. 3a) to 34.6% (34.1%) in the near-term (Fig. 3b–e), 44.4% (47.6%) in the mid-term (Fig. 3c–f), and 52.7% (56.7%) in the long-term (Fig. 3d–g), under SSP2-4.5 (SSP5-8.5). For the LSM-HVPD type (top-left quadrant), the probability also rise from the present-day 17.8% (Fig. 3a) to 24.2% (23.4%) in the near-term (Fig. 3b–e), 26.7% (28.3%) in the mid-term (Fig. 3c–f), and 52.7% (56.7%) in the long-term (Fig. 3c–f), under SSP2-4.5 (SSP5-8.5). Correspondingly, the probabilities of the low VPD-dominated types (HSM-LVPD and LSM-LVPD) would decline consistently. Compatible with results in Fig. 2, the probabilities of low SM types (LSM-HVPD and LSM-LVPD) vary slightly, with approximately 40% for each period under two emission scenarios.

3.2. *Response of dryland GPP loss to severe drought stress*

How will dryland GPP respond to the intensifying drought stress under future warming? We address this question by employing the GPP loss from nine CMIP6 ESMs. At the global scale, the annual aggregated

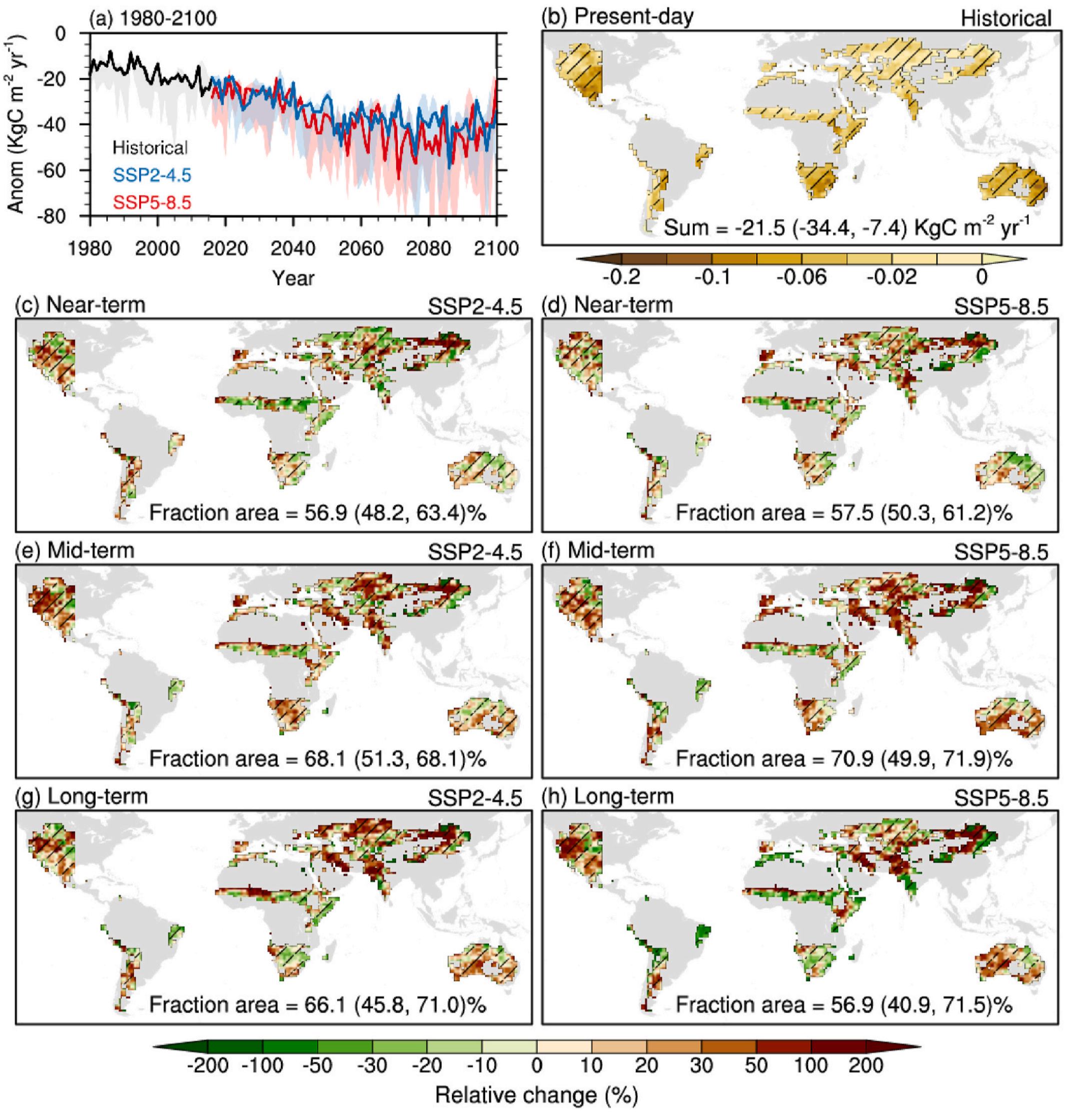

Fig. 4. Changes in annual GPP anomaly associated with severe drought (SPEI ≤ -1.5) across global vegetated drylands simulated by nine CMIP6 ESMs. (a) Time series of annual aggregated GPP anomalies (unit: KgC m^{-2} yr^{-1}) during 1980–2 100. Historical simulations (black) and future projections under SSP2-4.5 (blue) and SSP5-8.5 (red) scenarios are illustrated in median (solid lines) and inter-quartile ranges (shadings). (b) Spatial pattern of annual GPP anomalies (unit: KgC m^{-2} yr^{-1}) over the present-day period (1995–2014). The numbers are the multi-model ensemble (MME), minimum and maximum for the annual aggregated GPP anomalies. (c–h) Spatial pattern of relative changes (unit: %) in annual GPP anomaly for the near-term (2021–2040, c–d), mid-term (2041–2060, e–f), and long-term (2081–2100, g–h) period, respectively, under SSP2-4.5 (c, e, g) and SSP5-8.5 (d, f, h) scenarios, with respect to the present-day baseline (b). The numbers are the multi-model ensemble (MME), minimum and maximum for the fractional area of global vegetated drylands where severe drought-associated GPP reduction is projected to exacerbate. Slant hatchings denote where six of nine models agree in the sign of relative changes.

dryland GPP losses associated with severe drought are projected to intensify gradually with warming, with a significant tendency of -0.24 KgC m^{-2} yr^{-1} in MME under SSP2-4.5 and -0.30 KgC m^{-2} yr^{-1} under SSP5-8.5, respectively (Fig. 4a). Regionally, the strengthening (negative values) GPP losses are especially remarkable over the Asian, North American and Australian drylands, while weakening (positive values) over the Southern African and South Asian regions (Fig. S5).

With respect to the present-day baseline (Fig. 4b), the spatial distributions of relative changes in annual GPP deviations linked with severe drought conditions over each specific period are further illustrated in Fig. 4c–h. We specially quantify the fractional areas of positive percentage values, indicating an aggravating GPP loss, with respect to the whole vegetated dryland areas. Under SSP2-4.5 (SSP5-8.5) scenario, the annual GPP loss linked with severe drought will further deteriorate over 56.9% (57.5%) of the whole vegetated drylands in the near-term period (Fig. 4c and d), 68.1% (70.9%) in the mid-term (Fig. 4e and f), and 66.1% (56.9%) in the long-term period (Fig. 4g and h), respectively, as estimated from MME. The largest risks in the severe drought-associated GPP reduction are expected to appear in the southern North American, South African, and Australian dryland areas in the mid-term (Fig. 4e and f), with the magnitude in GPP loss exceeding double of the present-day baseline. It is noticeable that the dryland GPP reductions stagnate and even reverse between the mid-term and long-term periods under SSP5-8.5 (Fig. 4a), which mainly occurs over the Northeast Asian, South Asian, Sahel and South African drylands (Fig. 4g and h). These regions are also expected to see robust wetting in SM (Fig. 2d) and relatively lower drought risks (Fig. 1e), because of strong increase in precipitation under high emission scenario (Ukkola et al., 2020; Cook et al., 2020), and thus favoring GPP surplus.

To examine the impact of drought stress changes on dryland productivity, we assess the GPP anomalies via binning the VPD and SM anomalies associated with severe drought for each grid cell (same as Fig. 3), as illustrated in Fig. 5. At present-day, the maximum annual drought-associated GPP losses exceeding 1.0 KgC m^{-2} yr^{-1} appears in

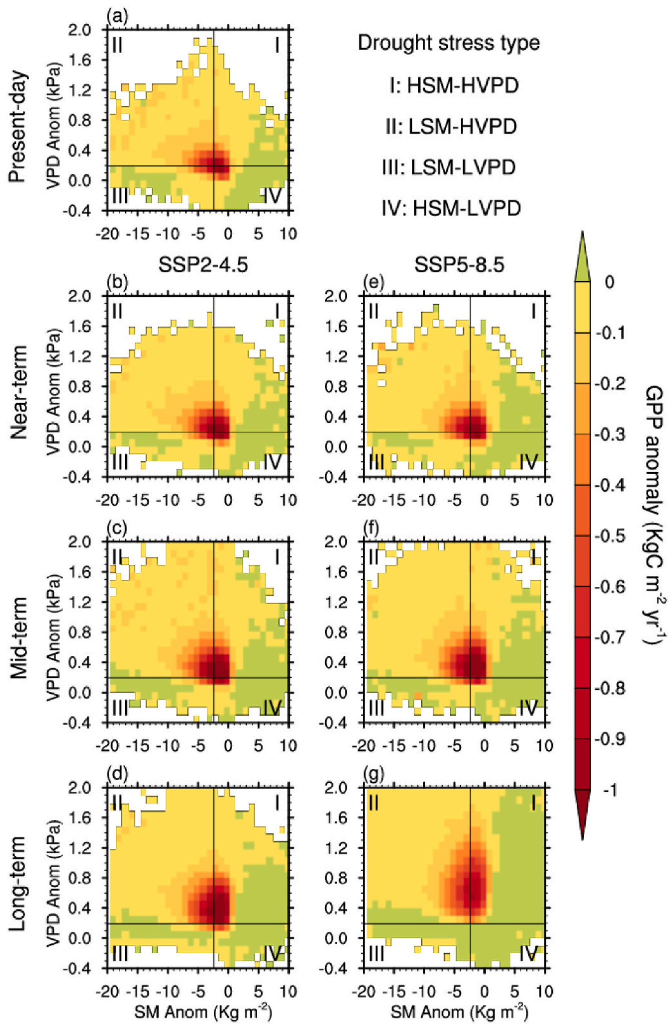

Fig. 5. Multi-model ensemble mean of annual dryland GPP anomaly (units: KgC m^{-2} yr^{-1}) for each bin of SM and VPD anomalies associated with severe drought events (SPEI ≤ -1.5) under SSP2-4.5 (b–d) and SSP5-8.5 (e–g) scenarios simulated by nine CMIP6 ESMs. The four specific periods, four drought stress categories and thin black lines are the same as Fig. 3.

the intersection of average SM and VPD anomalies (Fig. 5a). Generally, the present-day maximum GPP reduction tends to shift and extend towards high VPD anomaly with time and warming (Fig. 5 and Fig. S6), highly consistent with that in the bivariate PDF distributions for SM and VPD anomalies (Fig. 3). In the long-term period (Fig. 5d–g and Figs. S6d and g), the maximum GPP losses are expected to occur with the associated VPD anomaly rising to 0.3–0.8 hPa (0.6–1.2 hPa) under SSP2-4.5 (SSP5-8.5). The results suggest more adverse impacts induced by higher atmospheric aridity on dryland productivity in a warming climate.

We further quantify the annual aggregated dryland GPP deviations linked with the four specific drought stress types (Fig. 6). On the whole, the annual aggregated GPP reduction in drylands will rise to 1.3 (1.28) times of the present-day baseline in the near-term, 1.71 (1.87) times in the mid-term, and 1.94 (2.19) times in the long-term period, under SSP2-4.5 (SSP5-8.5) scenario, respectively (purple bars in Fig. 6). Align with the increasing probabilities for the high VPD-dominated (HSM-HVPD and LSM-HVPD) drought stress (Fig. 3), the dryland GPP losses induced by the two types are projected to aggravate dramatically, reaching 2.46–3.45 times of the present-day reduction in the long-term period (orange and pink bars in Fig. 6). In addition, the percentage of GPP reduction linked with the two types will rise substantially from the present-day 67.7%–78.6% (78.6%) in the near-term, 88.0% (91.4 %) in the mid-term, and 95.2% (101.7%) in the long-term period under SSP2-4.5 (SSP5-8.5) scenario. Notably, it is the LSM-HVPD type (pink bars in Fig. 6), with the second-most probability of four severe drought stress, that contributes the largest fractional GPP losses. For the two low VPD-dominated types (LSM-LVPD and HSM-LVPD), the dryland GPP loss (negative anomaly) caused by drought is expected to decline consistently from the present-day 15–16% of the total GPP reductions to minor (~2%) in the long-term period under SSP2-4.5, and may even reverse, leading to a weak GPP surplus (positive anomaly), under SSP5-8.5 (green and blue bars in Fig. 6), highly identical to the results in Figs. 4 and 5.

4. Summary and discussion

In this study, we investigated the changes in two drought stressors of dryland ecosystems under a warming climate and quantified their impacts on dryland GPP deviations. The conclusions are summarized as follows.

The CMIP6 ESMs project an increasing in the intensity, affected area and occurrence of severe drought events (SPEI-06 ≤ -1.5) across global vegetated drylands. Although severe drought-associated SM deficits exhibit a mild alleviation, the high VPD aggravates substantially under intermediate (SSP2-4.5) and high (SSP5-8.5) emission scenarios. Regarding bivariate PDFs for SM and VPD anomalies, severe drought stress across global vegetated drylands was further categorized into four specific types. The probabilities of high VPD-dominated types (HSM-HVPD and LSM-HVPD) are projected to substantially increase from the present-day 39% to nearly 90% (82.5–92.4%) in the long-term period under the two scenarios.

The annual GPP losses induced by severe drought stress are expected to deteriorate over more than half fraction (56.9–70.9%) of global vegetated drylands, particularly in the southern North American, South African, and Australian areas. The annual aggregated dryland GPP reduction associated with severe drought in the long-term period would be approximately 2.0 (2.1–2.37) times of the present-day level of ~21.5 KgC m^{-2} yr^{-1}. Furthermore, the GPP losses linked with the high VPD-dominated drought stress contribute to the majority of the total dryland GPP reduction, with their proportions increasing from the present-day 67.7%–95.2% (101.7%) in the long-term period under SSP2-4.5 (SSP5-8.5) scenario.

One limitation of our analysis is the fixed extent of global drylands without considering the types of terrestrial ecosystems. Drylands identified by AI are expected to expand under climate warming (Fu and Feng, 2014; Huang et al., 2016; Yao et al., 2020), and plants regulate their response divergently to drought stress according to their specific biochemical and physiological functions (Gupta et al., 2020; Flach et al., 2021; Zhang H et al., 2022). Moreover, the mechanisms of plant modulation under rising drought stress and CO_2 concentrations are more complex due to the interactions between these drivers and processes (Sang et al., 2021; McDowell et al., 2022). For instance, we excluded the CO_2 fertilization by subtracting a running 30-year GPP climatology following Xu et al. (2019) and Gonsamo et al. (2021), but this method can not eliminate the influences of CO_2 on water use efficiency (Peters et al., 2018; Zhang et al., 2019; Wang et al., 2022). As for the two drought stressors, the land-atmosphere feedbacks are enhanced in drylands, further exacerbating the severity and propagation of compound soil drought and atmospheric aridity (Huang et al., 2017; Schumacher et al., 2022).

Our findings reveal an increasingly prevalent and widespread risk of high VPD-dominated drought stress to dryland ecosystems with global warming, which is essential for global carbon uptake (Wang et al., 2022). Moreover, high atmospheric aridity conditions also pose great challenges associated with wildfire disasters to both natural and human environments (Jain et al., 2022; Jones et al., 2022). Special attention should be paid to those hotspots that would be threatened by exacerbating severe drought stress due to both decreasing SM and elevating

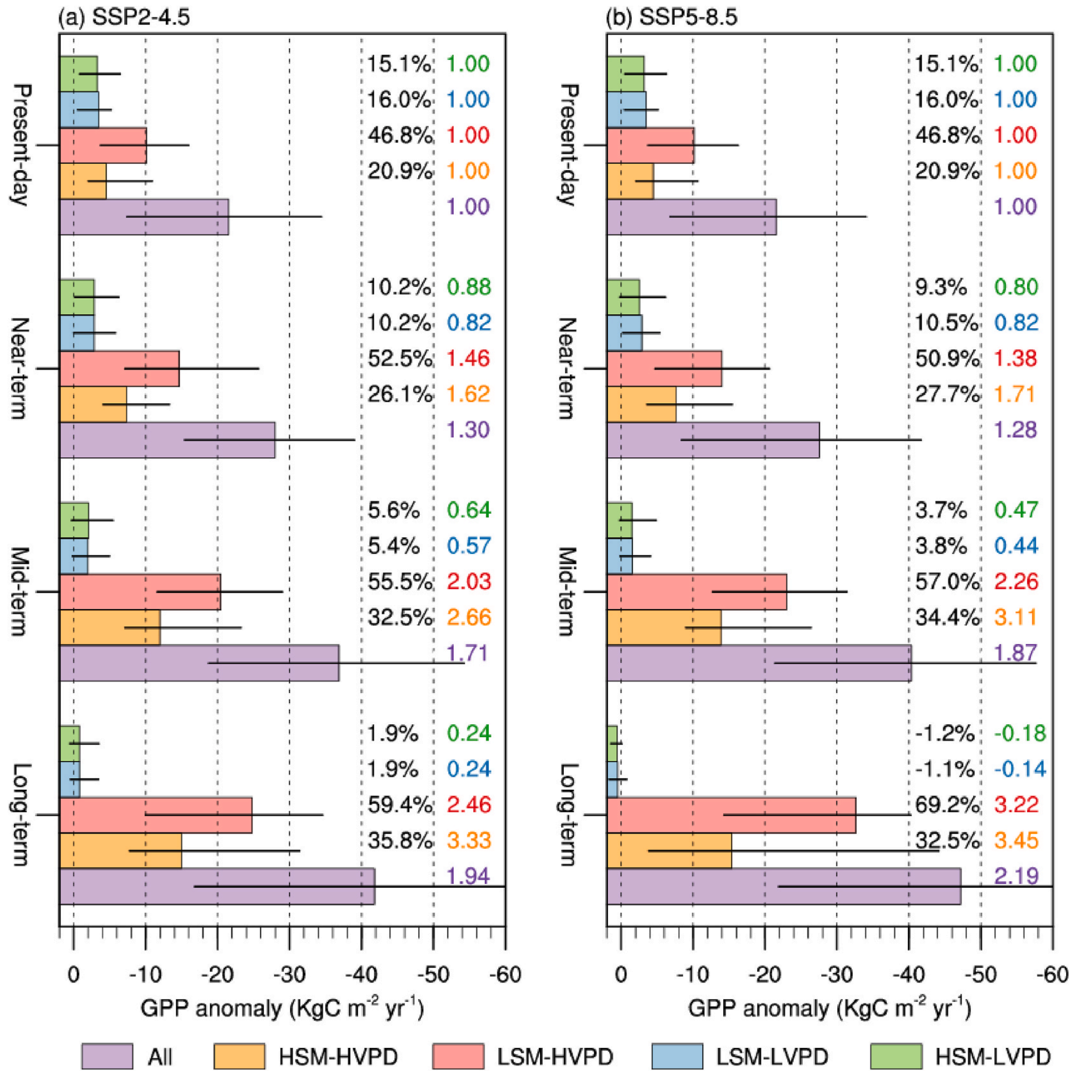

Fig. 6. Changes in annual aggregated dryland GPP deviations (unit: KgC m^{-2} yr^{-1}) associated with different drought stress types under SSP2-4.5 (a) and SSP5-8.5 (b) scenarios simulated by nine CMIP6 ESMs. The four specific periods and four drought stress categories are the same as Fig. 3. The bars and thin lines refer to the multi-model ensemble (MME), minimum and maximum for the annual aggregated GPP anomalies. The black numbers are the percentage of GPP deviations linked with each drought stress type with respect to their total values (purple, Fig. 4) for each period, and the color numbers are the relative magnitude of GPP deviations for each period with respect to their respective present-day baseline.

VPD. These vulnerable areas include the southern North American, South African, and Australian drylands. These regions are mainly covered by grasslands and croplands (Fig. S1) and are highly sensitive to drought extremes (Gampe et al., 2021). The drought-induced reduction in dryland vegetation productivity could have detrimental socio-economic effects by impacting ecosystem services, including reducing cropland production and cattle grazing, further hindering the achievement of SDGs in drylands (Fu et al., 2021). Thereby, to reduce threats from environmental degradation and guarantee stable food security in drylands, we underscore the need to deploy adaptation measures to intensify drought resilience of natural and cultivated vegetation through genetic, chemical and microbial approaches (Zhang H et al., 2022; Tarolli and Zhao, 2023; Novick et al., 2024). Such adaptations could aid in planning and management to achieve more resilient and sustainable outcomes in a changing climate.

CRediT authorship contribution statement

Xiaojing Yu: Conceptualization, Data curation, Formal analysis, Funding acquisition, Investigation, Methodology, Writing – original draft. **Lixia Zhang:** Conceptualization, Funding acquisition, Methodology, Supervision, Writing – review & editing. **Tianjun Zhou:** Methodology, Validation, Formal analysis. **Jianghua Zheng:** Methodology, Validation. **Jingyun Guan:** Data curation, Validation.

Declaration of competing interest

The authors declare that they have no known competing financial interests or personal relationships that could have appeared to influence the work reported in this paper.

Data availability

Data will be made available on request.

Acknowledgements

This study is supported by the National Natural Science Foundation of China (Grants 42305184 and 42075037). We acknowledge the High Performance Computer resources (2023-EL-PT-000184) from the National Key Scientific and Technological Infrastructure project "Earth System Numerical Simulation Facility" (EarthLab).

Appendix A. Supplementary data

Supplementary data to this article can be found online at https://doi.org/10.1016/j.wace.2024.100692.

Supporting information

Additional supporting information may be found online in the Supporting Information section.

References

Allen, R.G., Pereira, L.S., Raes, D., Smith, M., 1998. Crop Evapotranspiration—Guidelines for Computing Crop Water Requirements-FAO Irrigation and Drainage Paper 56, vol. 300. FAO, Rome, p. 6541.

Berg, A., Sheffield, J., 2018. Climate change and drought: the soil moisture perspective. Curr. Clim. Change Rep. 4 (2), 180–191. https://doi.org/10.1007/s40641-018-0095-0.

Berg, A., et al., 2016. Land–atmosphere feedbacks amplify aridity increase over land under global warming. Nat. Clim. Change 6, 869–874. https://doi.org/10.1038/nclimate3029.

Boucher, O., Servonnat, J., Albright, A.L., Aumont, O., Balkanski, Y., Bastrikov, V., et al., 2020. Presentation and evaluation of the IPSL-cm6a-LR climate model. J. Adv. Model. Earth Syst. 12, e2019MS002010 https://doi.org/10.1029/2019MS002010.

Cao, D., Zhang, J., Han, J., et al., 2022. Projected increases in global terrestrial net primary productivity loss caused by drought under climate change. Earth's Future 10, e2022EF002681. https://doi.org/10.1029/2022EF00268.

Chen, D., et al., 2021. Framing, context, and methods. In: Masson-Del-motte, V., Zhai, P., Pirani, A., et al. (Eds.), Climate Change 2021: the Physical Science Basis. Contribution of Working Group I to the Sixth Assessment Report of the Intergovernmental Panel on Climate Change. Cambridge University Press, Cambridge, United Kingdom and New York, NY, USA, pp. 147–286. https://doi.org/10.1017/9781009157896.003.

Cherchi, A., Fogli, P.G., Lovato, T., et al., 2019. Global mean climate and main patterns of variability in the CMCC-CM2 coupled model. J. Adv. Model. Earth Syst. 11 (1), 185–209. https://doi.org/10.1029/2018MS001369.

Cook, B.I., Mankin, J.S., Marvel, K., Williams, A.P., Smerdon, J.E., Anchukaitis, K.J., 2020. Twenty-first century drought projections in the CMIP6 forcing scenarios. Earth's Future 8, e2019EF001461. https://doi.org/10.1029/2019EF001461.

Cox, P., Jones, C., 2008. Climate change - illuminating the modern dance of climate and CO_2. Science 321, 1642–1644.

Davies, J., Barchiesi, S., Ogali, C.J., Welling, R., Dalton, J., Laban, P., 2016. Water in Drylands: Adapting to Scarcity through Integrated Management. IUCN, Gland, Switzerland.

Döscher, R., et al., 2022. The EC-earth3 Earth system model for the coupled model intercomparison project 6. Geosci. Model Dev. (GMD) 15, 2973–3020. https://doi.org/10.5194/gmd-15-2973-2022.

Eyring, V., et al., 2016. Overview of the coupled model intercomparison project Phase 6 (CMIP6) experimental design and organization. Geosci. Model Dev. (GMD) 9, 1937–1958. https://doi.org/10.5194/gmd-9-1937-2016.

Fang, Z., Zhang, W., Brandt, M., Abdi, A.M., Fensholt, R., 2022. Globally increasing atmospheric aridity over the 21st century. Earth's Future 10, e2022EF003019. https://doi.org/10.1029/2022EF003019.

Flach, M., et al., 2021. Vegetation modulates the impact of climate extremes on gross primary production. Biogeosciences 18, 39–53. https://doi.org/10.5194/bg-18-39-2021.

Friedl, M., Sulla-Menashe, 2015. D. MCD12C1 MODIS/Terra+Aqua land cover type yearly L3 global 0.05Deg CMG V006. NASA EOSDIS Land Processes DAAC). https://doi.org/10.5067/MODIS/MCD12C1.006.

Fu, Q., Feng, S., 2014. Responses of terrestrial aridity to global warming. Journal of Geophysical Research Atmospheres 119, 7863–7875. https://doi.org/10.1002/2014JD021608.

Fu, B., et al., 2021. The Global-DEP conceptual framework — research on dryland ecosystems to promote sustainability. Curr. Opin. Environ. Sustain. 48, 17–28. https://doi.org/10.1016/j.cosust.2020.08.009.

Gampe, D., Zscheischler, J., Reichstein, M., et al., 2021. Increasing impact of warm droughts on northern ecosystem productivity over recent decades. Nat. Clim. Change 11, 772–779. https://doi.org/10.1038/s41558-021-01112-8.

Gentine, P., Green, J.K., Guerin, M., et al., 2019. Coupling between the terrestrial carbon and water cycles-a review. Environ. Res. Lett. 14, 083003 https://doi.org/10.1088/1748-9326/ab22d6.

Gonsamo, A., Ciais, P., Miralles, D.G., et al., 2021. Greening drylands despite warming consistent with carbon dioxide fertilization effect. Global Change Biol. 27, 3336–3349. https://doi.org/10.1111/gcb.15658.

Green, J.K., Seneviratne, S.I., Berg, A.M., et al., 2019. Large influence of soil moisture on long-term terrestrial carbon uptake. Nature 565, 476–479. https://doi.org/10.1038/s41586-018-0848-x.

Grossiord, C., Buckley, T.N., Cernusak, L.A., et al., 2020. Plant responses to rising vapor pressure deficit. New Phytol. 226, 1550–1566. https://doi.org/10.1111/nph.16485.

Gupta, et al., 2020. The physiology of plant responses to drought. Science 368, 266–269.

Hammond, W.M., et al., 2022. Global field observations of tree die-off reveal hotter-drought fingerprint for Earth's forests. Nat. Commun. 13, 1761. https://doi.org/10.1038/s41467-022-29289-2.

Harris, I., Osborn, T.J., Jones, P., Lister, D., 2020. Version 4 of the CRU TS monthly high-resolution gridded multivariate climate dataset. Sci. Data 7, 109. https://doi.org/10.1038/s41597-020-0453-3.

He, B., Wang, S., Guo, L., Wu, X., 2019. Aridity change and its correlation with greening over drylands. Agric. For. Meteorol. 278, 107663 https://doi.org/10.1016/j.agrformet.2019.107663.

He, B., et al., 2022. Worldwide impacts of atmospheric vapor pressure deficit on the interannual variability of terrestrial carbon sinks. Natl. Sci. Rev. 9, nwab150 https://doi.org/10.1093/nsr/nwab150.

He, P., Han, Z., He, M., et al., 2023. Atmospheric dryness thresholds of grassland productivity decline in China. J. Environ. Manag. 338, 117780 https://doi.org/10.1016/j.jenvman.2023.117780.

Huang, J., Yu, H., Guan, X., Wang, G., Guo, R., 2016. Accelerated dryland expansion under climate change. Nat. Clim. Change 26, 1–7. https://doi.org/10.1038/NCLIMATE2837.

Huang, J., Li, Y., Fu, C., Chen, F., Fu, Q., Dai, A., et al., 2017. Dryland climate change: recent progress and challenges. Rev. Geophys. 55, 719–778. https://doi.org/10.1002/2016RG000550.

Hulme, M., 1996. Recent climatic change in the world's drylands. Geophys. Res. Lett. 23, 61–64. https://doi.org/10.1029/95GL03586.

Humphrey, V., Berg, A., Ciais, P., et al., 2021. Soil moisture–atmosphere feedback dominates land carbon uptake variability. Nature 592, 65–69. https://doi.org/10.1038/s41586-021-03325-5.

Jain, P., et al., 2022. Observed increases in extreme fire weather driven by atmospheric humidity and temperature. Nat. Clim. Change 12, 63–70.

Jones, M.W., Abatzoglou, J.T., Veraverbeke, S., et al., 2022. Global and regional trends and drivers of fire under climate change. Rev. Geophys. 60, e2020RG000726 https://doi.org/10.1029/2020RG000726.

Jung, M., Koirala, S., Weber, U., et al., 2019. The FLUXCOM ensemble of global land-atmosphere energy fluxes. Scitific Data 6, 74. https://doi.org/10.1038/s41597-019-0076-8.

Kendall, M.G., 1955. Rank correlation methods. British J Psychol 25, 86–91.

Kimm, H., et al., 2020. Redefining droughts for the U.S. Corn Belt: the dominant role of atmospheric vapor pressure deficit over soil moisture in regulating stomatal behavior of maize and soybean. Agric. For. Meteorol. 287, 107930 https://doi.org/10.1016/j.agrformet.2020.107930.

Li, H., Li, Z., Chen, Y., Xiang, Y., Liu, Y., Kayumba, P.M., Li, X., 2021. Drylands face potential threat of robust drought in the CMIP6 SSPs scenarios. Environ. Res. Lett. 16, 114004 https://doi.org/10.1088/1748-9326/ac2bce.

Liu, L., Gudmundsson, L., Hauser, M., Qin, D., Li, S., Seneviratne, S.I., 2020. Soil moisture dominates dryness stress on ecosystem production globally. Nat. Commun. 11, 4892. https://doi.org/10.1038/s41467-020-18631-1.

Lobell, D.B., et al., 2014. Greater sensitivity to drought accompanies maize yield increase in the US Midwest. Science 344, 516–519. https://doi.org/10.1126/science.1251423.

Mann, H.B., 1945. Non-parametric tests against trend. Econometrica 13, 163–171.

Mauritsen, T., Bader, T., Becker, T., Behrens, J., Bittner, M., Brokopf, R., et al., 2019. Developments in the MPI-M Earth system model version 1.2 (MPI-ESM1.2) and its response to increasing CO_2. J. Adv. Model. Earth Syst. 11 (4), 998–1038. https://doi.org/10.1029/2018MS001400.

McDowell, N.G., 2011. Mechanisms linking drought, hydraulics, carbon metabolism, and vegetation mortality. Plant Physiology 155, 1051–1059.

McDowell, N., Pockman, W.T., Allen, C.D., et al., 2008. Mechanisms of plant survival and mortality during drought: why do some plants survive while others succumb to drought? New Phytol. 178, 719–739. https://doi.org/10.1111/j.1469-8137.2008.02436.x.

McDowell, N.G., Sapes, G., Pivovaroff, A., et al., 2022. Mechanisms of woody-plant mortality under rising drought, CO_2 and vapour pressure deficit. Nat. Rev. Earth Environ. 3, 294–308.

Middleton, N.J., Thomas, D.S.G., 1992. UNEP: World Atlas of Desertification. Edward Arnold, Sevenoaks.

Monteith, J.I.L., 1965. Evaporation and Environment, vol. 19. Symposia of the Society for Experimental Biology, pp. 205–234.

Novick, K.A., Ficklin, D.L., Grossiord, C., et al., 2024. The impacts of rising vapour pressure deficit in natural and managed ecosystems. Plant Cell Environ. 1–29. https://doi.org/10.1111/pce.14846.

O'Neill, B.C., et al., 2016. The scenario model intercomparison project (ScenarioMIP) for CMIP6. Geosci. Model Dev. (GMD) 9, 3461–3482. https://doi.org/10.5194/gmd-9-3461-2016.

O'Neill, B.C., et al., 2017. The roads ahead: narratives for shared socioeconomic pathways describing world futures in the 21st century. Global Environ. Change 42, 169–180. https://doi.org/10.1016/j.gloenvcha.2015.01.004.

Penman, H.L., 1948. Natural evaporation from open water, bare soil and grass. Proceedings of The Royal Society A 193, 120–145.

Perkins-Kirkpatrick, S.E., Lewis, S.C., 2020. Increasing trends in regional heatwaves. Nat. Commun. 11, 3357. https://doi.org/10.1038/s41467-020-16970-7.

Peters, W., van der Velde, I.R., van Schaik, E., et al., 2018. Increased water-use efficiency and reduced CO_2 uptake by plants during droughts at a continental scale. Nature Geosci 11, 744–748. https://doi.org/10.1038/s41561-018-0212-7.

Piao, S., Zhang, X., Chen, A., Liu, Q., Lian, X., Wang, X., Peng, S., Wu, X., 2019. The impacts of climate extremes on the terrestrial carbon cycle: a review. Sci. China Earth Sci. 62, 1551–1563. https://doi.org/10.1007/s11430-018-9363-5.

Reichstein, M., et al., 2013. Climate extremes and the carbon cycle. Nature 500, 287–295. https://doi.org/10.1038/nature12350.
Running, S.W., 2008. Ecosystem disturbance, carbon, and climate. Science 321, 652–653.
Sang, Y., et al., 2021. Recent global decline of CO_2 fertilization effects on vegetation photosynthesis. Science 373, 1295–1300.
Schumacher, D.L., Keune, J., Dirmeyer, P., et al., 2022. Drought self-propagation in drylands due to land-atmosphere feedbacks. Nat. Geosci. 15, 1–7.
Sen, P.K., 1968. Estimates of the regressions coefficient based on Kendall's tau. J Amer Statis Asso 63, 1379–1389.
Seneviratne, S.I., et al., 2021. Weather and climate extreme events in a changing climate. In: Masson-Del-motte, V., Zhai, P., Pirani, A. (Eds.), Climate Change 2021: the Physical Science Basis. Contribution of Working Group I to the Sixth Assessment Report of the Intergovernmental Panel on Climate Change. Cambridge University Press, Cambridge, United Kingdom and New York, NY, USA, pp. 1513–1766. https://doi.org/10.1017/9781009157896.013 et al.
Swart, N.C., Cole, J.N.S., Kharin, V.V., et al., 2019. The Canadian Earth system model version 5 (CanESM5.0.3). Geosci. Model Dev. (GMD) 12 (11), 4823–4873. https://doi.org/10.5194/gmd-12-4823-2019.
Tarolli, P., Zhao, W., 2023. Drought in agriculture: preservation, adaptation, migration. The Innovation Geoscience, 1 (1), 100002. https://doi.org/10.59717/j.xinn-geo.2023.100002.
Theil, H., 1992. A rank-invariant method of linear and polynomial regression analysis. In: Henri Theil's Contributions to Economics and Econometrics. Springer, Netherlands, pp. 345–381.
Ukkola, A.M., De Kauwe, M.G., Roderick, M.L., et al., 2020. Robust future changes in meteorological drought in CMIP6 projections despite uncertainty in precipitation. Geophys. Res. Lett. 47, e2020GL087820 https://doi.org/10.1029/2020GL087820.
Vicente-Serrano, S.M., Beguería, S., López-Moreno, J.I., 2010. A multiscalar drought index sensitive to global warming: the standardized precipitation evapotranspiration index. J. Clim. 23, 1696–1718. https://doi.org/10.1175/2009JCLI2909.1.
Vicente-Serrano, S.M., et al., 2013. Response of vegetation to drought time-scales across global land biomes. Proceedings of the National Academy of Sciences of the United States of America 110, 52–57. https://doi.org/10.1073/pnas.1207068110.
Wang, L., Jiao, W., MacBean, N., et al., 2022. Dryland productivity under a changing climate. Nat. Clim. Change 12, 981–994. https://doi.org/10.1038/s41558-022-01499-y.
Wang, S., Fu, B., Wei, F., et al., 2023. Drylands contribute disproportionately to observed global productivity increases. Sci. Bull. 68, 224–232. https://doi.org/10.1016/j.scib.2023.01.014.
White, R.P., Nackoney, J., 2003. Drylands, People, and Ecosystem Goods and Services: a Web-Based Geospatial Analysis. World Resources Institute, Washington, DC, USA.
Wu, T., Lu, Y., Fang, Y., et al., 2019. The Beijing Climate center climate system model (BCC-csm): the main progress from CMIP5 to CMIP6. Geosci. Model Dev. (GMD) 12 (4), 1573–1600. https://doi.org/10.5194/gmd-12-1573-2019.
Xu, C., McDowell, N.G., Fisher, R.A., et al., 2019. Increasing impacts of extreme droughts on vegetation productivity under climate change. Nat. Clim. Change 9, 948–953. https://doi.org/10.1038/s41558-019-0630-6.
Xu, S., Gentine, P., Li, L., Wang, L., Yu, Z., Dong, N., et al., 2023. Response of ecosystem productivity to high vapor pressure deficit and low soil moisture: lessons learned from the global eddy-covariance observations. Earth's Future 11, e2022EF003252. https://doi.org/10.1029/2022EF003252.
Yao, J., Liu, H., Huang, J., et al., 2020. Accelerated dryland expansion regulates future variability in dryland gross primary production. Nat. Commun. 11, 1665. https://doi.org/10.1038/s41467-020-15515-2.
Yi, C., et al., 2022. Tree mortality in a warming world: causes, patterns, and implications. Environ. Res. Lett. 17, 030201 https://doi.org/10.1088/1748-9326/ac507b.
Yu, X., Zhang, L., Zhou, T., Zhang, X., 2023. Long-term changes in the effect of drought stress on ecosystems across global drylands. Sci. China Earth Sci. 66 (1), 146–160. https://doi.org/10.1007/s11430-022-1001-0.
Yu, X., Zhang, L., Zhou, T., Zheng, J., 2024. Assessing performances of CMIP6 models in reproducing droughts across global drylands. Adv. Atmos. Sci. 41 (2), 193–208. https://doi.org/10.1007/s00376-023-2278-4.
Yuan, W., et al., 2019. Increased atmospheric vapor pressure deficit reduces global vegetation growth. Sci. Adv. 5, eaax1396 https://doi.org/10.1126/sciadv.aax1396.
Zhang, Q., et al., 2019. Response of ecosystem intrinsic water use efficiency and gross primary productivity to rising vapor pressure deficit. Environ. Res. Lett. 14, 074023 https://doi.org/10.1088/1748-9326/ab2603.
Zhang, H., Zhu, J., Gong, Z., et al., 2022. Abiotic stress responses in plants. Nature Review Genetics 23, 104–119. https://doi.org/10.1038/s41576-021-00413-0.
Zhang, Y., Piao, S., Sun, Y., et al., 2022. Future reversal of warming-enhanced vegetation productivity in the Northern Hemisphere. Nat. Clim. Chang. 12, 581–586. https://doi.org/10.1038/s41558-022-01374-w.
Zhang, L.X., Yu, X.J., Zhou, T.J., et al., 2023. Understanding and attribution of extreme heat and drought events in 2022: current situation and future challenges. Adv. Atmos. Sci. 40, 1941–1951. https://doi.org/10.1007/s00376-023-3171-x.
Zhong, Z., He, B., Wang, Y., et al., 2023. Disentangling the effects of vapor pressure deficit on northern terrestrial vegetation productivity. Sci. Adv. 9, eadf3166 https://doi.org/10.1126/sciadv.adf3166.
Zhou, S., et al., 2019a. Land-atmosphere feedbacks exacerbate concurrent soil drought and atmospheric aridity. Proc. Natl. Acad. Sci. USA 116, 18848–18853. https://doi.org/10.1073/pnas.1904955116.
Zhou, S., Zhang, Y., Williams, A.P., Gentine, P., 2019b. Projected increases in intensity, frequency, and terrestrial carbon costs of compound drought and aridity events. Sci. Adv. 5, eaau5740 https://doi.org/10.1126/sciadv.aau5740.